Acoustic observations of lava fountain activity during the 2021 Fagradalsfjall eruption, Iceland

Oliver D. Lamb[1*], Julia E. Gestrich[2], Talfan D. Barnie[3], Kristín Jónsdóttir[3], Cécile Ducrocq[4], Michael J. Shore[1], Jonathan M. Lees[1] and Stephen J. Lee[5]

[1*]Dept. of Earth, Marine and Environmental Sciences, University of North Carolina at Chapel Hill, Chapel Hill, NC, USA.
[2]Alaska Volcano Observatory, Geophysical Institute, University of Alaska Fairbanks, Fairbanks, AK, USA.
[3]Icelandic Met Office, Reykjavik, Iceland.
[4]Nordic Volcanological Centre, Institute of Earth Sciences, University of Iceland, Reykjavik, Iceland.
[5]US Army Research Laboratory, Army Research Office, Durham, NC, USA.

*Corresponding author(s). E-mail(s): olamb@email.unc.edu;
Contributing authors: jegestrich@alaska.edu; talfan@vedur.is; kristin.jonsdottir@vedur.is; cad7@hi.is; mshore@email.unc.edu; jonathan.lees@unc.edu; stephen.j.lee28.civ@mail.mil;

Abstract

The 2021 eruption within the Fagradalsfjall volcanic system in Iceland provided a rare opportunity to record acoustic data generated by a basaltic fissure. Eruptive activity in May 2021 was defined by a sequence of repetitive lava fountaining activity. Here we describe key observations and analysis conducted on acoustic data recorded by a four-element infrasound microphone array near the eruption site. Detailed inspection of acoustic waveforms and comparisons with seismic data and lava fountain height measurements revealed a complex eruptive sequence during each lava fountain event: acoustic tremor during peak lava fountaining was followed by a transition to Strombolian-style activity with distinct high-amplitude impulsive waveforms. Quantitative comparisons to jet noise spectra finds complex turbulence acoustics during each event, with evidence of variations in the wavefield centred on peak lava fountain heights. Strombolian explosions could mostly be modelled by oscillations of bursting gas slugs at the top the magma column, with a minor number of events exhibiting Helmholtz resonance behaviour instead. We find an increase in bubble radii between early and late May, suggesting a widening of the upper conduit during

the lava fountain sequence. Finally, we propose that higher acoustic amplitudes, in addition to a wider conduit in late May, indicates higher gas flux through the conduit culminating in shorter lava fountain events. This study highlights the value of deploying acoustic sensors for providing additional constraints on eruption dynamics and source parameters during effusive fissure eruptions in Iceland and elsewhere.

Keywords: Acoustics, Fagradalsfjall, Iceland, lava fountain, Jet noise, Strombolian

1 Introduction

Atmospheric acoustic signals with frequencies ranging from 0.02 to 20 Hz are classified as infrasound and are regularly documented during volcanic activity (Johnson and Ripepe, 2011; Fee and Matoza, 2013). These atmospheric perturbations may be generated by processes including short-duration explosions, sustained volcanic jets, and mass flows. Localisation and quantification of acoustics during eruptions can provide information on shallow processes within the conduit and above the vent. Therefore, the deployment of microphones around an active volcano can provide additional insights into activity not readily available by other means.

Relative to other types of eruptive activity such as Strombolian and Vulcanian, acoustic records of basaltic fissure eruptions with Hawaiian-style lava fountains are rare with previous studies limited to events at Etna (Cannata et al, 2009, 2011) and Kīlauea volcanoes (Fee et al, 2011; Lyons et al, 2021; Gestrich et al, 2021). Acoustic activity during these events are usually manifested as semi-continuous tremor with broadband frequency spectra characteristics. Using sensor arrays and networks, it is possible to track the activity progression along fissures, including the opening of new vents (Cannata et al, 2011; Fee et al, 2011), and quantifying the effusion rate of high-speed, highly channelised lava flows (Lyons et al, 2021). Acoustic source processes at the vent(s) during fissure eruptions have been modelled as either Strombolian-style explosions (Cannata et al, 2011) or a sustained jet flow (Gestrich et al, 2021).

Low viscosity magma allows large gas bubbles to ascend through the magma column and manifest at the surface as distinct, impulsive, high amplitude Strombolian bursts. During this type of activity, at least two different acoustic source processes have been described. Firstly, strong gas bubble oscillation immediately prior to bursting at the lava surface generates an m-shaped waveform where the positive peaks are less intense than the negative peak (Vergniolle and Brandeis, 1996; Vergniolle et al,

1996, 2004). Secondly, longer harmonic waveforms with an exponentially decaying coda are linked to Helmholtz resonance of gas within or above the bubble (Vergniolle and Caplan-Auerbach, 2004; Cannata et al, 2009; Fee et al, 2010b; Goto and Johnson, 2011). Modelling of Strombolian acoustics allows for quantitative estimates of parameters such as bubble radius, bubble length, and overpressure (Vergniolle et al, 1996, 2004; Vergniolle and Caplan-Auerbach, 2004). During the 2008 flank fissure eruption at Etna volcano, both the bubble oscillation and Helmholtz resonance source model were detected (Cannata et al, 2009). For different vents across the fissure, waveform inversions for bubble oscillations produced estimated bubble radii of 2–3.5 m with bubble lengths of 7.2–7.6 m (Cannata et al, 2009, 2011). In contrast, events generating Helmholtz resonance were modelled by bubbles of 6 m radius and up to 40 m length (Cannata et al, 2009).

Recent studies have demonstrated how eruptions can generate an infrasonic form of 'jet noise' such as those generated by small-scale anthropogenic jet flows (e.g. Matoza et al, 2009; Fee et al, 2010a; Matoza et al, 2013; McKee et al, 2017; Gestrich et al, 2021). Anthropogenic jet noise refers to sounds generated by turbulent exhaust (i.e. a jet flow) exiting aircraft or rocket engines and have been studied in detail for engineering investigations (e.g. Tam, 1998). Two distinct components of jet noise have been recognised: large-scale turbulence (LST) and fine-scale turbulence (FST; Tam, 2019). FST is associated with fine-scale eddies generating acoustics, whereas LST is generated by instability waves forming at the margin of the jet flow (Tam, 2019). LST sound radiation is highly directional but may be reduced for volcanoes due to higher temperature jets and a strong diffraction at lower frequencies (Matoza et al, 2009). Jet noise frequency spectra exhibit self-similarity, with spectral shape remaining relatively constant and scaling with frequency, diameter, and velocity (Tam, 1998). Studies have shown that this self-similarity can extend to volcanic length scales (metres to hundreds of metres), therefore, similar relationships may exist between volcanic jet noise spectra and vent diameter, jet velocity, and temperature (Matoza et al, 2009, 2013; McKee et al, 2017; Gestrich et al, 2021). While the spectral shapes are similar, the peak frequencies at volcanoes are generally lower and can be explained through the Strouhal number, a non-dimensional parameter used to describe oscillating flow (Seiner, 1984). Quantitative comparisons of similarity spectra were carried out on acoustics recorded during the 2018 Kīlauea fissure eruption in which included 80 m high lava fountains (Gestrich et al, 2021). Changes in misfits between the recorded acoustic spectra versus the similarity spectra coincided

with variations in eruption dynamics, supporting possible quantitative estimation of eruption flow features (Matoza et al, 2013; McKee et al, 2017; Gestrich et al, 2021).

In this paper, we describe acoustics recorded during the 2021 fissure eruption of Fagradalsfjall, Iceland. In particular, we focus on repetitive lava fountaining that characterised the eruptive activity in May. Each lava fountain was defined by a sequence of activity that can be described by jetting followed by distinct Strombolian explosions (see movie S1 for an example event). Isolation and careful analysis of acoustics during the lava fountaining permits quantification of vent dimensions and highlights the value of acoustic monitoring for future basaltic fissure eruptions.

2 Fagradalsfjall eruption

After a protracted period of earthquake activity on the Reykjanes peninsula in SW Iceland, an eruption began at the Fagradalsfjall volcanic system on March 19 2021 (Barsotti et al, 2022), the first such eruption on the peninsula for nearly 800 years (Sæmundsson et al, 2020). The eruption continued until September 18 2021, at which point the lava flow field had covered an area of 4.8 km^2 with an estimated bulk volume of 0.15 km^3 (Pedersen et al, 2021). Eruptive activity in March and April was spread over 9 distinct vents across a NNE-SSW trending line of 800 m length (Fig. 1a). From the late April until the end of the eruption, activity was focused from a single vent (Vent 5 in Barsotti et al, 2022), which we will refer to as the 'main' vent for the remainder of this article. From approximately 01:00 UTC on 2 May, the eruptive activity was characterised by a sequence of repetitive lava fountaining of up to 200 m height above the vent (Fig. 1b; Barsotti et al, 2022). This period coincided with peak discharge rate of lava from the eruption of 12–13 $m^3 \cdot s^{-1}$ (Pedersen et al, 2021). Variations in duration, repose intervals, and heights of the lava fountaining was observed throughout May and into early June, eventually transitioning into discontinuous lava outpouring that defined the remainder of the eruption (Barsotti et al, 2022). Seismic data analysis (Eibl et al, 2022) and FTIR gas emission measurements (Scott et al. *in prep.*) have suggested the presence of a shallow cavity (<500 m) beneath the vent where repeated foam collapse in the magma may be driving the distinctive lava fountaining activity.

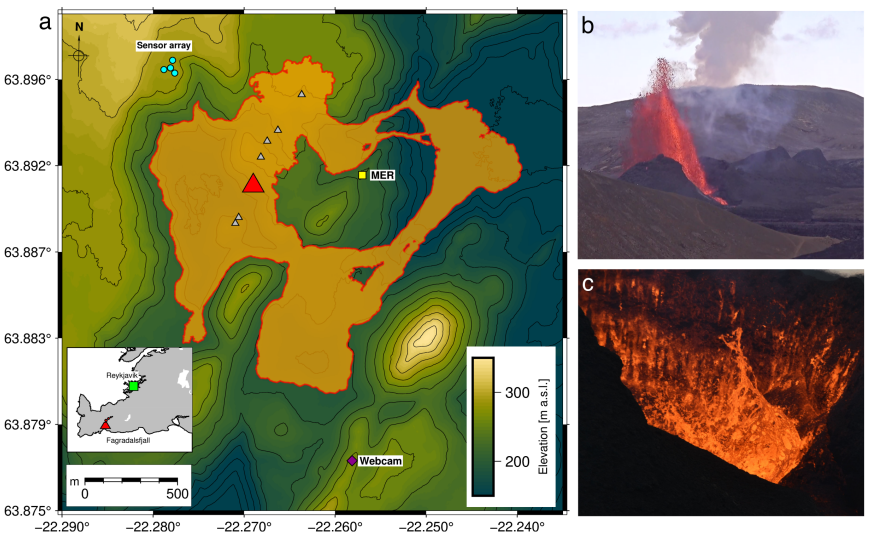

Fig. 1 (a) Map showing the location of the microphone array (blue circles) with respect to the main vent (red triangle) and lava flow area on 3 May (orange area; Pedersen et al, 2021). Also marked are locations of other vents that were no longer active by May (grey triangles), the MER seismic station (yellow square), and the webcam used for estimating lava fountain heights (purple diamond). DEM is from ArcticDEM (Porter et al, 2018, modified by the National Land Survey of Iceland, 2020). Inset: Map of SW Iceland showing the Reykjanes Peninsula with locations of the eruption site and Reykjavik metropolitan area indicated. (b) Example of a lava fountain event at 11:07 UTC on 5 May, as recorded by the webcam located in panel a. (c) Example of a Strombolian explosion on 11 May at the end of a lava fountain event. Photo captured from vantage point 500 m SSE of the vent with 150 mm lens.

3 Data and Methods

3.1 Acoustic array and processing

The infrasound data presented in this study are from a four-element campaign array installed on 21 April approximately 800 m north-west of what would eventually be the main vent (Fig. 1a). The 70 m aperture array was equipped with four InfraBSU V2 infrasound sensors (flat response from 0.1 to >40 Hz; Marcillo et al, 2012) with one co-located 4.5 Hz geophone (not used here) connected to DiGOS DATA-CUBE^3 digitisers recording data at 200 Hz. We estimated a theoretical uncertainty in back-azimuth of 4–5° and trace velocity of 18–22 m·s^{-1} for this array configuration (Szuberla and Olson, 2004). Sensor locations were estimated using time-averaged locations from a handheld GPS receiver. The array ran almost continuously until 30 August, with the exception of 8–17 May when the array had to be removed due to brush fires triggered by the eruption. Technical issues with the sensors from 21 to 23 May led to incorrect values of acoustic pressure levels being recorded, therefore

data recorded during this period could only be used for the detection of coherent signals and not for quantifying source parameters. We compare acoustics with seismicity recorded at station MER located NE of the main vent (Fig. 1a), which used a LE-3D/5s seismometer recording data at 100 Hz.

Before processing, the acoustic data were filtered with a Butterworth bandpass filter at 0.5–20 Hz. The lower boundary was chosen to remove a strong micro-barom signal, and the upper boundary was chosen to ensure as much of the eruptive signal was recorded while removing anthropogenic noise interference (e.g. helicopters; Barsotti et al, 2022). The data was processed with a least-squares beamforming algorithm (Szuberla and Olson, 2004) to identify coherent signals in 10 s windows with 50% overlap. Signals associated with eruptive activity were identified using back-azimuths from 122–162°, trace velocities of 250–400 $m{\cdot}s^{-1}$, and a median cross-correlation maximum of >0.5. To track the number of lava fountaining events occurring during our time periods of analysis, we defined an 'event' as a time period when a coherent eruption signal was detected for continuous periods of >60 s and followed by repose intervals of >60 s. For each 10 s window with an identified eruption signal, relative infrasound energy (E_a) was calculated by integrating squared pressure over time (Fee et al, 2013; Lyons et al, 2021):

$$E_a = \int_0^T \Delta p^2(t) dt \tag{1}$$

We follow the reasoning of Lyons et al (2021) by using relative acoustic energy because jet noise was a significant component of the wavefield during peak lava fountaining (see section 4.2). Therefore, we cannot assume simple spherical acoustic radiation pattern and any measure of energy or intensity on a single array will be relative to itself. Estimating absolute acoustic energy would require observations from multiple arrays at different distances, azimuths, and heights relative to the source (Matoza et al, 2013).

3.2 Lava fountain height estimations

Lava fountain heights can be estimated from video camera image analysis by developing a kymograph (e.g. Witt and Walter, 2017). Kymographs were developed for lava fountain events on 5 and 18 May using video recorded by a camera installed on top of Langihryggur approximately 2 km SE of the main vent by Ríkisútvarpið (RÚV), the Icelandic National Broadcasting Service (Fig. 1a). Images were recorded at 25 fps and lava fountain heights were estimated in each frame relative to sea level.

See supplementary information for a full description of how lava fountain heights were estimated. As the camera view angle cannot see the base of the vent (Fig. 1b), we plot lava fountain heights relative to the lowest section of the breach in the SE section of the cone, which was estimated as 238 m a.s.l.

3.3 Jet noise similarity spectra fitting

To quantify the presence of jet noise in acoustics generated during lava fountaining activity at Fagradalsfjall, we used an approach recently developed to analyse acoustics during the 2018 Kīlauea eruption (Gestrich et al, 2021). Here we provide a brief description of this approach; see Gestrich et al (2021) for a detailed method description and discussion.

The similarity spectra (i.e. the model spectra) for LST (S_{LST}) and FST (S_{FST}) are defined as the following (Tam et al, 1996):

$$S_{LST} = \underbrace{A\left(\frac{r}{D_j}\right)^{-2}}_{C_{LST}} \cdot F\left(\frac{f}{f_L}\right) \tag{2}$$

$$S_{FST} = \underbrace{B\left(\frac{r}{D_j}\right)^{-2}}_{C_{FST}} \cdot G\left(\frac{f}{f_F}\right) \tag{3}$$

where f is the frequency, D_j is the fully expanded diameter of the jet, r is the source-receiver distance (800 m), and A and B are the amplitudes of the large-scale and fine-scale structures, respectively. The first half the right-hand side of each equation is redefined to C_{LST} and C_{FST}, respectively, so that only one numerical value defines the amplitude of each similarity spectrum. F and G are the spectrum functions of the large-scale and fine-scale structures, respectively, and are dependent on the peak frequency for LST (f_L) and FST (f_F), which ultimately define the characteristic shape of each similarity spectra. In general, LST has a narrower frequency spectrum than FST (Tam, 2019).

To fit the similarity spectra with the frequency spectrum of the recorded acoustic data, we use a least-squares method called Trust Region Reflective Algorithm. We use the root mean squared deviation ($RMSD$) to quantify the difference between the similarity spectrum S and the data spectrum d, defined as (Gestrich et al, 2021):

$$RMSD = \sqrt{\frac{1}{n}\sum^{n}(S_i - d_i)^2} \tag{4}$$

Results are presented within the decibel scale (dB, relative to $(20\mu\text{Pa})^2/\text{Hz}$). Due to the complexity of the acoustic spectra during each lava fountain event, we focus on using multiple overlapping frequency bands to fit the models to the data and calculate the corresponding RMSD values. This results in a misfit spectrum for both FST and LST, and subtracting the difference between the two produces a misfit difference spectrogram which shows which of each model is more appropriate for the data over time and different frequency bands. For the jet noise analysis, we limit the frequency bands to the 0.15-20 Hz range using 15 s windows with 90% overlap.

3.4 Bubble burst modelling

Examinations of the acoustics recorded during the lava fountaining at Fagradalsfjall identified both bubble oscillation (Vergniolle and Brandeis, 1996; Vergniolle et al, 2004) and Helmholtz resonance (Vergniolle and Caplan-Auerbach, 2004) events. Here we describe the method used to describe and quantify the waveforms. A full description of the models can be found in Appendix A.

Waveform inversions were carried out on bubble bursts manually picked from the acoustic record at Fagradalsfjall and we used an approach similar to that described for modelling acoustics recorded during the Bogoslof eruption (Lyons et al, 2019). For bubble oscillation events, we calculated 10^5 synthetic waveforms from unique combinations of bubble overpressure ΔP (5–80 kPa), initial bubble radius R_o (0.1–10 m), and bubble length L (5–200 m), and solved equation (A1) with a Runge-Kutta ordinary differential equation solver. For Helmholtz resonance events, we calculated 10^5 synthetic waveforms using equation (A6) and directly cross-correlated each with the observed acoustic waveform. The ranges used for the variables were: 50–1x10^4 Pa for ΔP, 0.5–15 m for R_{hole}, and 5–200 m for L. The ranges of each value for each model were chosen based on preliminary testing of the models against selected waveforms. Each synthetic waveform was then directly compared with the observed acoustic waveform and was considered a match if they fell within $\pm 5\%$ of the observed peak-to-peak pressure and the cross-correlation coefficient maximum was ≥ 0.8. This approach differed slightly for Helmholtz resonance events, as the first (i.e. maximum) peak in the synthetic waveform is an overestimation due to the assumption the hole radius in the bubble membrane is instantaneously reached (Vergniolle and Caplan-Auerbach, 2004). Therefore, we measured synthetic peak-to-peak pressures by ignoring the first 'peak' in the waveform. For each picked bubble event, this method produces a subset of synthetic waveform matches from which we use the median and median absolute

deviation values to estimate best-fit bubble parameters and their variability, respectively. This approach results in non-unique solutions for each picked bubble event but these estimations fully explore the model space and may provide insights into changes in bubble source parameters over time.

4 Results

Due to brush fires forcing a temporary removal of the array, as well as technical issues (section 3.1), we cannot present a continuous acoustic record of the Fagradalsfjall lava fountain activity through all of May 2021. Here we focus on two time periods and present key observations and analysis from each: 2–8 and 17–24 May; hereafter we will refer to each period as 'early' and 'late' May, respectively.

4.1 General observations

Acoustics recorded during early and late May indicate distinct differences in lava fountaining activity (Fig. 2) with longer events in the former time period relative to the latter. In general, eruptive acoustics appear with high amplitudes relative to the background activity with peak amplitudes generally occurring at the midpoint or end of each lava fountain event. Acoustic amplitudes in early May generally peak at $\leq$10 Pa (Fig. 2a), whereas amplitudes in late May reached up to and over 20 Pa (Fig. 2c). The frequency content of each fountaining event was generally broadband and may be described as acoustic tremor (Fig. 2b, d) with peak frequencies within 0.5–2.5 Hz.

Array processing results indicate broad fluctuations in lava fountaining activity (Fig. 3). In all, we detected 609 and 1087 lava fountaining events in early and late May, respectively, corresponding to an average lava fountain rate of ∼4.2 and ∼6 events per hour. Event durations in early May generally followed a downward trend, falling from <1000 s down to ∼300 s (Fig. 3a). A break in this trend occurred on early 5 May, when several events occurred with durations up to <2000 s. Simultaneously, repose intervals followed a generally increasing trend, rising from <100 to ∼300 s (Fig. 3b). One notable feature is an apparent diurnal variation in repose intervals (and in durations to a lesser degree), with lower values appearing daily at 00:00–06:00 UTC. We observe an apparent correlation with wind velocities recorded at the eruption site (Fig. S1 in supplementary materials) suggesting reduced signal-to-noise ratios due to wind noise; lower signal-to-noise ratios increase the apparent time interval between lava fountain events. For late May, lava fountaining event durations are shorter and

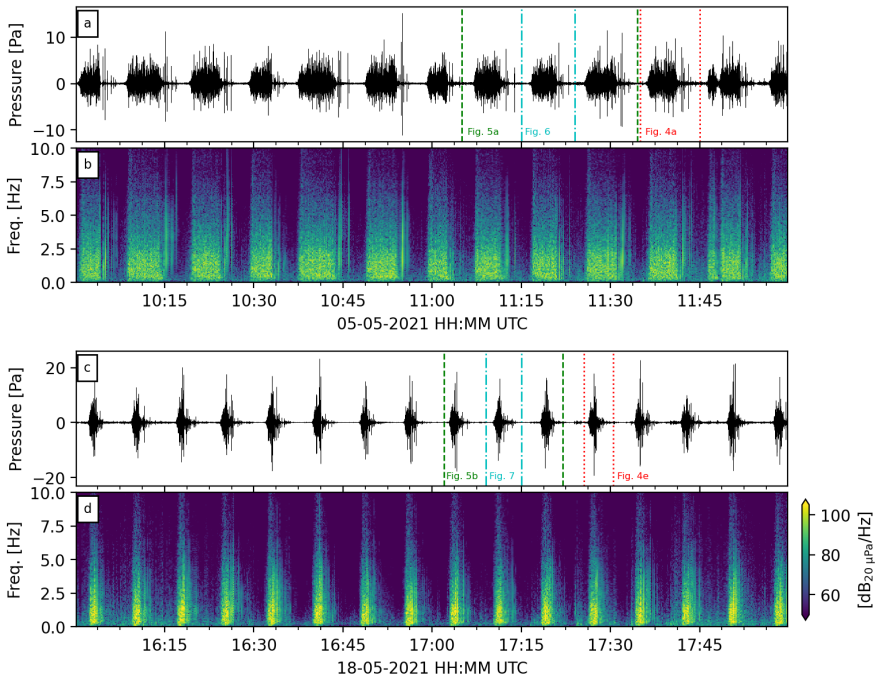

Fig. 2 Examples of acoustic waveforms (a, c) and their respective frequency spectrograms (b, d) recorded during lava fountain sequences on 5 May (a,b) and 18 May (c,d). Dotted lines in panels a and c delineate time periods detailed in Figs. 4–7.

are somewhat more stable with only a slight downward trend from 200 to 100 s (Fig. 3d). Repose intervals between events are longer, fluctuating between 300 to 400 s length, but show no clear indication of any diurnal fluctuations (Fig. 3e). Larger acoustic amplitudes in late May (Fig. 2c) have likely reduced the impact of wind noise on signal-to-noise ratios. Estimated relative acoustic energies during early May show a rising trend in energies over time, from an average of 6.7 $Pa^2 \cdot s$ to 25.8 $Pa^2 \cdot s$ (Fig. 3c). This latter value was sustained on late 17 May, but power levels became more erratic before technical issues affected the sensors at the array (Fig. 3f). Higher relative acoustics energies of up to 50 $Pa^2 \cdot s$ were estimated after the sensor issues were resolved.

Close inspection of acoustics recorded during individual lava fountaining events and direct comparisons with seismicity generated by the same events indicates a complex activity sequence (Fig. 4). In both early and late May, acoustics and seismicity generated during lava fountain events appear almost simultaneously (Fig. 4a, c, e and g). Due to the emergent nature of their onsets, it is challenging to quantify whether there is any significant time lag between the acoustics and seismicity.

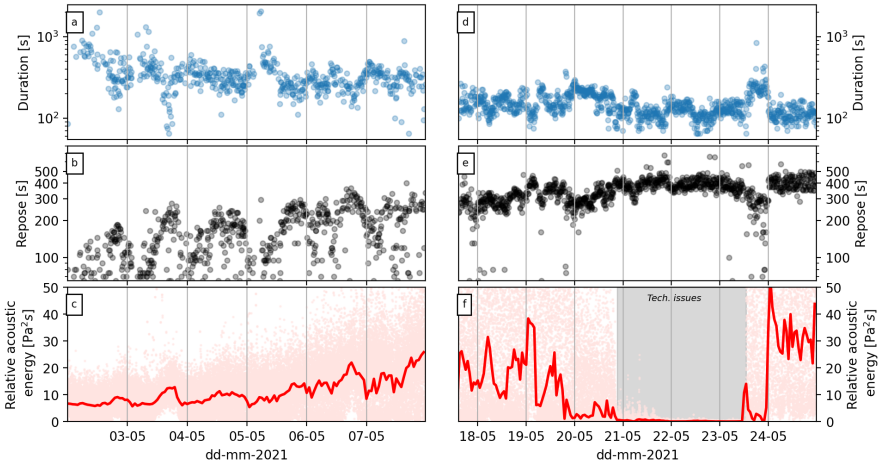

Fig. 3 Durations (a,d) and repose intervals (b,e) of lava fountain events, and relative acoustic energies (c,f) for 10 s detection window during two time periods: (a-c) 2–8 May, (d-f) 17–25 May.

The first stage of each fountain event is defined by a sustained acoustic tremor with frequencies peaking at <2.5 Hz (Fig. 4a,b, e and f). As noted previously, the highest acoustic amplitudes are associated with impulsive events with peak frequencies ranging up to 3 Hz; we term these events 'bubble bursts' and describe them in detail below (section 4.3). One distinct difference between events during early and late May is the transition from the tremor to the bubble bursting. Acoustics in early May indicate a more sustained period of tremor for several minutes with multiple concurrent high amplitude bubble bursting events, followed by a rapid decrease in tremor and a sequence of impulsive events with generally decreasing amplitudes (Fig. 4a, b). In late May, the tremor stage is curtailed and is rapidly replaced by diminishing bubble bursting events (Fig. 4e, f). Seismic amplitudes and frequencies display a distinct difference with the acoustics in both early and late May (Fig. 4c, d, g and h). Amplitudes generally reached a peak in the first stage of the fountaining with slightly reduced amplitudes sustained for most of the fountaining event, before concluding with a second peak followed by gradual decrease to background levels (Fig. 4c, g). Notably, the second amplitude peak in seismicity appears after the conclusion of the acoustic tremor during each fountaining event. The frequency content of the seismicity during each fountaining event indicates faint harmonic tremor, with peaks appearing at ∼2.5, ∼5, and ∼7.5 Hz (Fig. 4d); these bands are not clear during fountaining events in late May. The distinct acoustic 'bubble-burst' events do not appear

clearly in the seismic data, although some peaks in the seismic 'coda' in early May could be related to this activity.

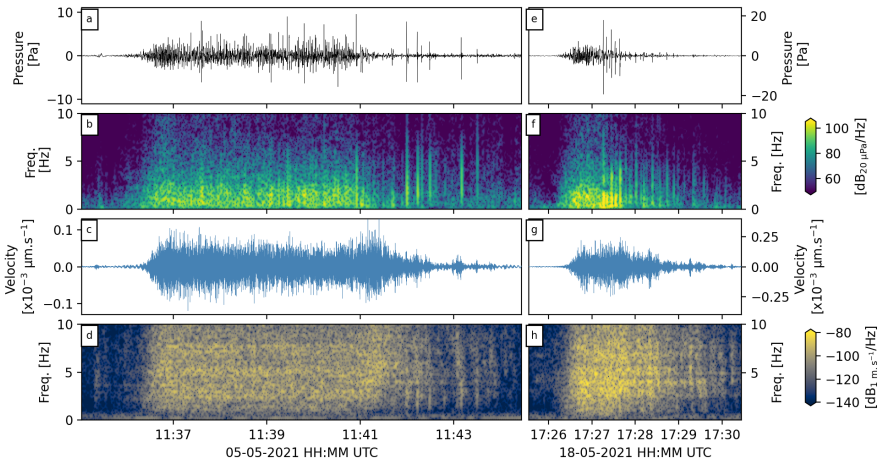

Fig. 4 Detailed view of acoustic (a, e) and seismic data (c, g) and their respective frequency spectrograms (b, f, d, h) recorded during lava fountain events on 05 (a-d) and 18 May (e-h). Acoustic data was recorded by one microphone of the array, and seismic data was recorded by a broadband sensor at MER (Fig. 1)

Further insights into the lava fountaining activity can be gleaned by comparing the acoustic and seismic recordings with the lava fountain heights estimated from webcam images (Fig. 5). To aid the comparison, we have plotted smoothed absolute acoustic and seismic amplitudes using a 10 s rolling window. Lava fountain heights during each time period of analysis generally display two different behaviours. In early May, lava fountaining quickly rises to reach a peak at 100–150 m in the first stage before a period of sustained low level fountaining fluctuating at 20–50 m (Fig. 5a). In late May, lava fountain heights quickly reach their peak values at 100–130 m but are instead followed by a rapid decrease down to low levels without any period of sustained fountaining (Fig. 5b). In both time periods, fountaining appears to commence almost simultaneously with the emergence of acoustic and seismic activity. However, the peak lava fountaining does not correlate with the highest amplitudes of the seismo-acoustic wavefield. Interestingly, decreases in lava fountain heights at the end of each event are simultaneous with decreases in acoustic amplitudes, but seismicity generally reach a peak amplitude following a time delay of $<$60 s.

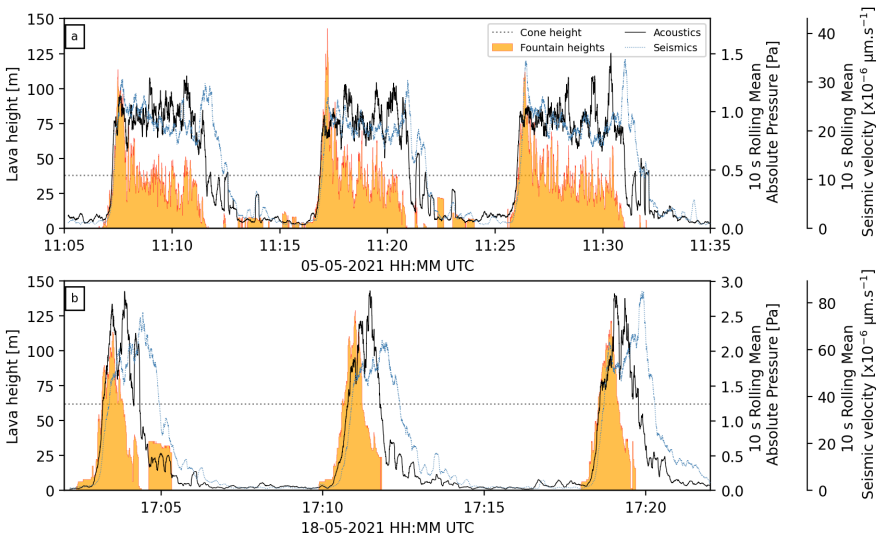

Fig. 5 Estimated lava fountain heights (orange area), mean absolute acoustic pressures (blue) and mean absolute seismic velocities (red) for two time periods on 05 May (a) and 18 May (b). Also marked are the estimated cone height on the day of each time period (black dotted line): 276 m a.s.l. for 05 May, and 300 m a.s.l for 18 May.

4.2 Turbulent acoustic tremor

The onset of each lava fountain event in May is defined by the emergence of acoustic tremor with peak frequencies <5 Hz (Fig. 4a, b, e and f). Here we present results from systematically quantifying the differences between the acoustic spectra and FST/LST similarity spectra (Figs. 6, 7; see Figs. S2–S5 in supplementary material for more examples). The misfit difference spectrograms indicate relatively strong LST turbulence before and after each lava fountain event (Fig. 6c, 7c). This is to be expected when background noise is typically comprised of turbulence generated by wind (e.g. Raspet and Webster, 2015). During each lava fountaining event, we find a generally bimodal distribution in the misfit spectra: FST is more dominant at >2 Hz, and LST is more dominant below. One notable departure from this distribution is the appearance of more dominant LST spectra at frequencies >5 Hz centred on the time of peak lava fountain heights during each event (Fig. 6c, 7c). FST spectra remained dominant in a small 'notch' at frequencies from 2–5 Hz. At frequencies <2 Hz, we observe complex fluctuations in the peak LST spectra during each event, with apparent upward 'gliding' during the bubble burst events (e.g. 17:12:15–17:13:20 in Fig. 7c).

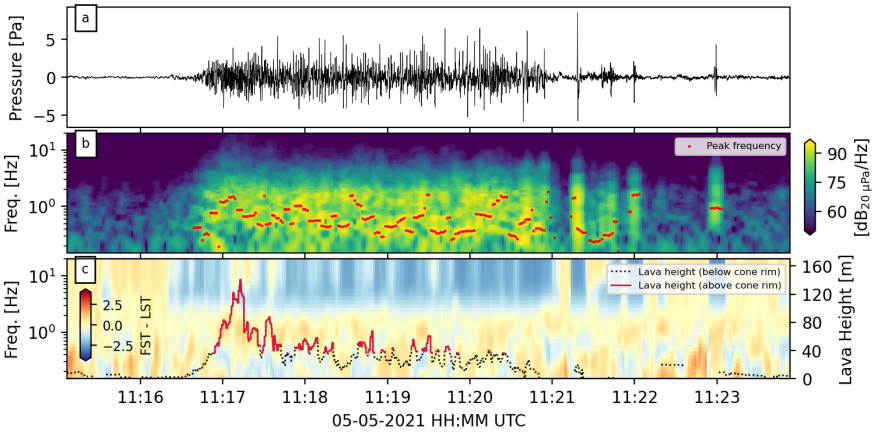

Fig. 6 Spectral quantification for a lava fountain event on 05 May. (a) Acoustic data as recorded at the array. (b) Frequency spectrogram for the data shown in panel a. Peak frequency through time is highlighted through time by red dots for each time window where max dB >75. Note that the spectrogram was built using longer time windows than those in Figs. 2 and 4, and the y-axis is plotted with a log-scale. (c) Misfit difference spectrogram plot showing times and frequencies of RMSD for FST (blue) and LST (red). Also plotted are measured lava fountain heights in black and red, with the latter colour indicating if this exceeds the measured lava cone height.

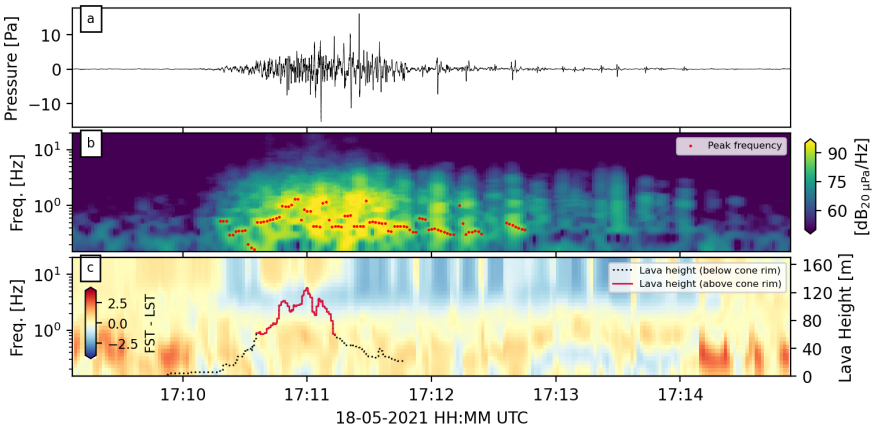

Fig. 7 Spectral quantification for a lava fountain event on 18 May. See Fig. 6 caption for details on panels.

4.3 Bubble burst modelling

The latter period of each lava fountain event is defined by sequences of impulsive bubble burst acoustics (Fig. 4). Bubble bursts during each time period of analysis was dominated by m-shaped waveforms linked to bubble oscillations (Fig. 8). In

comparison, events with Helmholtz resonance occur relatively rarely but a notable sequence was observed at 05:00 UTC on 05 May (Fig. 9).

Through inspection of the acoustic recordings, we manually picked 105 and 72 bubble burst events on 05 and 18 May, respectively. For events picked in early May, peak-to-peak amplitudes ranged from 0.42–23.0 Pa with 1.10–4.29 Hz peak frequencies. In comparison, events in late May had peak-to-peak amplitudes ranging from 0.69–36.54 Pa and 0.75–2.13 Hz peak frequencies. Across both time periods, we matched a subset of synthetic waveforms to all but 4 events in late May, with a minimum of 36, maximum of 4,389, and a median of 1573 matches (Fig. 8i - l; see Figs. S6 and S7 in supplementary material for more examples). Overall, the matched model parameters tended to span the boundary conditions without clustering near end-member values, indicating an acceptable range of initial conditions. However, we find poorly constrained bubble lengths, with median values falling at the midpoint of the boundary conditions with large median absolute deviations (Fig. 8b, f). Nevertheless, we find narrow distributions of initial radii (R_o; Fig. 8a, e) and overpressures (ΔP; Fig. 8d, h), therefore we interpret these parameters as well constrained. In early May, the initial radii range from 0.3 to 3.3 m (Fig. 8a), and overpressures range from 12 to 63 kPa (Fig. 8d). Despite the poor constraint on bubble lengths, we estimate bubble volumes using equation (A2) and find a range of 45–3017 m^3 (Fig. 8c). By comparison for late May, the initial radii tend to be larger with values from 0.7 to 4.5 m (Fig. 8e), overpressures are approximately similar with estimations from 13 to 56 kPa (Fig. 8g), and volumes are larger at 162–4900 m^3 (Fig. 8h).

As noted previously, bubble burst events displaying Helmholtz resonance waveforms are relatively rare. However, one sequence of bubble bursts at 05:48 UTC on 05 May was notable for their apparent resonant nature with upward frequency 'gliding' (Fig. 9a, b). This particular sequence occurred immediately after a time interval which featured one of the longest fire fountain events and one of the tallest lava fountain events observed (Fig. S8 in supplementary material). We manually picked 14 bubble burst events from the sequence which had 0.48–10.50 Pa peak-to-peak amplitudes and 1.92 to 4.49 Hz peak frequencies. We matched a subset of synthetics to all events, finding 20–1996 matches with a median of 147 (Fig. 9g, h; see Fig. S9 in supplementary material for all events). Similar to results of modelling bubble oscillation events, the matched model parameters tended to span the boundary conditions without clustering near end-member values, indicating an acceptable range of initial conditions. Manual inspection of the matched synthetics relative to the real waveforms finds a good match for the second to fourth peaks after the first, but poor

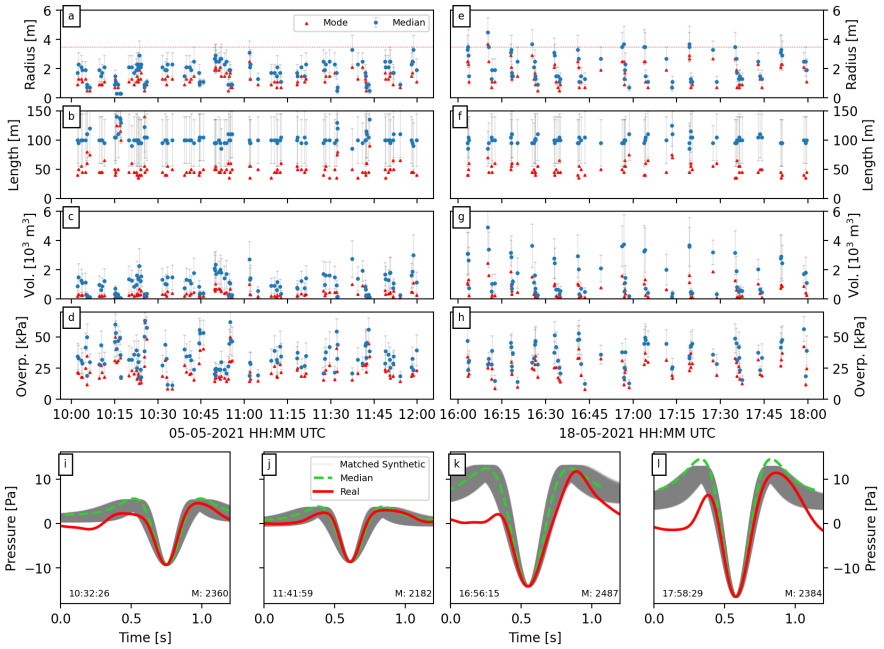

Fig. 8 Results of modelling oscillating events on May 5 and 18. (a - d) Median (blue dots) and modes (red triangles) of estimated radius, bubble length, bubble volume, and bubble overpressure, respectively, for each picked bubble burst on May 5. Error bars on the median values are the median absolute deviation values. (e - h) Same as panels a - d, except for events on May 18. Horizontal red line in panels a and e indicate upper conduit radius estimated from drone images on 5 May (Jöel Ruch, pers. communication). (i - l) Four examples of modelled oscillating bubble bursts (red lines) from May 5 (i and j) and May 18 (k and l), along with their matched synthetics (grey line) and the median synthetic waveform (green dashed line). The time of each example is noted in the bottom left, and the number of matched synthetics in the bottom right.

matching thereafter (e.g. Fig. 9g, h). We find narrow distributions of hole radii (R_{hole}; Fig. 9c) and overpressures (ΔP; Fig. 9f), therefore we interpret these parameters as relatively well constrained. Bubble lengths (L) do not tend to fall at the midpoint of the boundary conditions, but the median absolute deviations are still large (Fig. 9d). We find radii ranging from 1.7 to 4.1 m and bubble lengths ranging from 42.5 to 162.5 m. Using equation (A19), we estimate volumes of 1489.7–6265.8 m^3 (Fig. 9e). Lastly, overpressures ranged from a maximum of 3800 Pa down to 150 Pa at the end of bubble sequence.

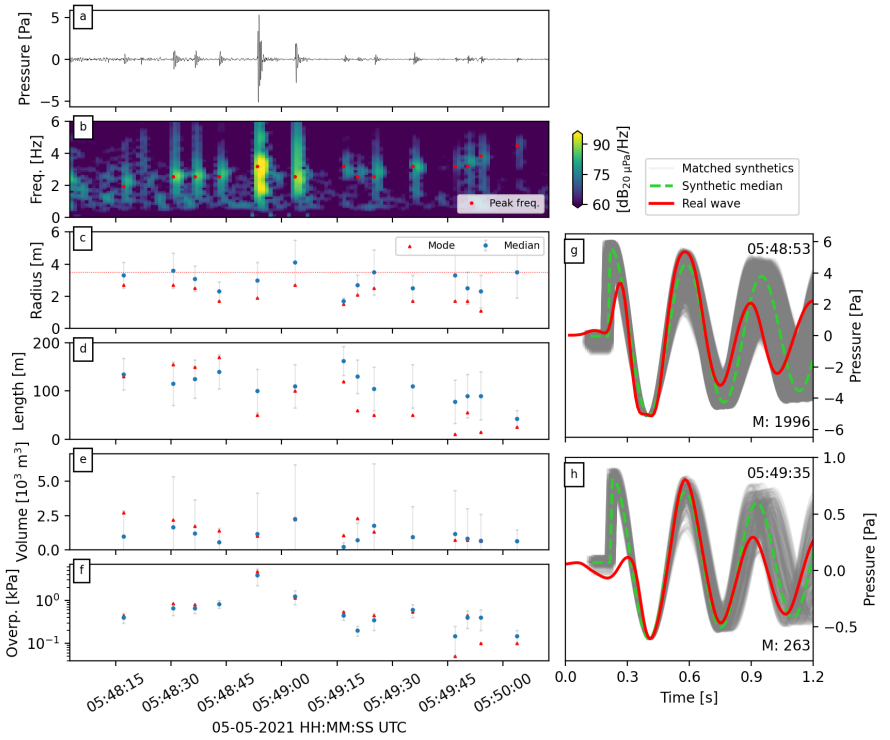

Fig. 9 Results of modelling bubble bursts with Helmholtz resonance on May 5. (a) Acoustic recording of sequence of bubble bursts displaying Helmholtz resonance on morning of May 5. (b) Frequency spectrogram of acoustic waveform in panel a. Also plotted are peak frequencies of bubbles manually picked from sequence (red dots). (c - f) Median (blue dots) and modes (red triangles) of estimated radius, bubble length, bubble volume, and bubble overpressure, respectively, for each bubble burst in the sequence. Error bars on the median values are the median absolute deviation values. Horizontal red line in panel c indicates upper conduit radius estimated from drone images on 05 May (Jöel Ruch, pers. communication). (g, h) Two examples of bubble bursts from the sequence in panel a (red lines), along with their matched synthetics (grey line) and the median synthetic waveform (green dashed line). The time and number of matched synthetics for each example is noted in the top and bottom right, respectively.

5 Discussion

The lava fountains observed at Fagradalsfjall were exceptional in terms of event lengths and their recurrence intervals. Previously documented lava fountains at Etna and Kīlauea were more prolonged (e.g. up to multiple months; Patrick et al, 2019; Lyons et al, 2021) and/or had longer repose intervals (e.g. days to weeks; Parfitt, 2004; Vergniolle and Ripepe, 2008). Acoustic data recorded during the lava fountains at Fagradalsfjall required multiple analytical tools to help discern the complex sequence of activity during each event.

Results from least-squares array processing found nearly 1700 individual lava fountaining events across two time periods of analysis in early and late May (Fig. 3). This amount approximately correlates with analysis carried out using seismic data (Eibl et al, 2022). The duration and repose intervals along with their broad fluctuations over time also correlate with the seismic analysis but we see an apparent diurnal cycle in early May due to lower signal-to-noise ratios from wind noise. Estimated relative acoustic energies in early May show an upward trend (Fig. 3c) that may reflect changes in eruptive activity over time. Analysis of acoustics from the 2018 eruption at Kīlauea have suggested that increases in acoustic energies correlate with increases in lava effusion rates over long time-scales (Patrick et al, 2019; Lyons et al, 2021). Time-averaged lava discharge rates compiled over the whole eruption suggest there was a rapid increase in late April and early May (Pedersen et al, 2021). Therefore we suggest the increase in relative energy in early May may be an approximate indicator of increases in lava effusion rates at Fagradalsfjall.

Closer inspection of acoustics generated during individual lava fountains suggest a general sequence of activity during each event: acoustic tremor is followed by a transition into and eventually superseded by impulsive bubble bursting (i.e. Strombolian) activity (Fig. 4). The apparent simultaneous increase of acoustic and seismic activity at the onset of each lava fountain event suggests both wavefields are, at first, generated by activity at or near the surface. However, the wavefields diverge at the end of each lava fountain event when a second peak seismic amplitude appears with a small time lag after acoustic amplitudes decline (Figs. 4, 5). The lack of higher acoustic amplitudes at this time suggests a sub-surface process with no atmospheric coupling. It is not clear what this process may be and further detailed analysis of seismicity is beyond the ambit of this article. Nevertheless, it is clear that while seismic data can be used to visualise overall trends in lava fountaining (e.g. Eibl et al, 2022), it may overestimate activity durations and underestimate repose intervals due to 'overshooting' of vent activity (Fig. 5). Another notable observation was peak acoustic amplitudes correlating with Strombolian activity instead of peak lava fountaining. Fluctuations in atmospheric pressure recorded by sensors at distance from a volcanic vent have been directly related to acoustic power, which depends strongly on the source radiation mechanism (Woulff and McGetchin, 1976). Three mechanisms are recognised: monopoles can be envisioned as an isotropically expanding source (i.e. an explosion), dipoles are equivalent to directional gas flux interacting with solid walls, and quadrupoles correspond to turbulent noise (i.e. a jet engine). Woulff and McGetchin (1976) use empirical constants on the order of 1, 10^{-2} and 10^{-5} for each

source, respectively. Thus, less acoustic power and lower acoustic amplitudes will be generated during the jetting phase (i.e. quadrupole) than the Strombolian phase (i.e. monopoles and/or dipoles) of each lava fountain event.

Jet noise similarity spectra fitting highlighted a complex distribution of FST and LST frequencies during each lava fountain event (Figs. 6, 7), with the former dominating at >2 Hz. The complexity of the acoustic wavefield is further highlighted when compared with analysis on acoustic data recorded during sustained lava fountaining at Kīlauea in 2018 (see Fig. 5 in Gestrich et al, 2021). While the link between changes in spectral properties of jet noise to eruption dynamics is an ongoing area of research (Gestrich et al. *in prep.*), here we see a potential connection with lava fountain heights. We noted the appearance of stronger LST turbulence at frequencies >5 Hz centred on the peak lava fountain heights during each event (Fig. 6c, 7c). LST sound radiation is highly directional, with a narrow cone-shaped wavefield pattern centred on the vent, but this cone may be enlargened for higher temperature and higher Mach number jets (Matoza et al, 2009; Viswanathan, 2009). The data presented here hints at an interaction between the cone morphology and the resulting turbulent wavefield, but we are wary in presenting an interpretation. Volcanic jetting is extremely complex and poorly understood compared to laboratory jets and modelling the complex wavefield generated during each fountaining event and how it may be affected by the growing cone is beyond the scope of this article. We also noted an upward 'gliding' feature in LST frequencies (<2 Hz) during the Strombolian events after each lava fountain event (e.g. Fig. 7c). We hypothesise that minor gas jetting occurred immediately after each Strombolian explosion, with higher frequencies caused by smaller slug volumes (Fig. 8c, g).

Inspection of the Strombolian explosions after each lava fountain event in early and late May revealed two kinds of bursting mechanism: bubble oscillation (Fig. 8) and Helmholtz resonance (Fig. 9). If we assume the R_{hole} parameter for the latter is approximately equivalent to R_o for the former, then the values of bubble radii for each type do roughly agree with each other on 5 May. These radii fall within the range of values found for Strombolian explosions at other volcanoes, including Stromboli, Etna, and Shishaldin (Vergniolle and Brandeis, 1996; Vergniolle et al, 2004; Vergniolle and Ripepe, 2008; Cannata et al, 2009). However, we find a poor constraint on bubble lengths with the bubble oscillation model with median values around the midpoint between bounds used for generating synthetics. If we instead look at the matching bubble length modal values, we find smaller values at 40–70 m which fall into the upper range of values found in previous studies. On the contrary,

overpressures are small compared to previous studies, with peak values at least one order of magnitude lower than the minimum values found at Shishaldin (Vergniolle et al, 2004). Analytical modelling of Strombolian eruptions finds a non-linear relationship between gas overpressure within slugs, and the total volume of the slug as well as thickness of magma between the slug and conduit walls (Del Bello et al, 2012). We note that estimated bubble volumes here are also relatively small compared to the previous studies, which may explain the low gas overpressure estimates. Even so, overpressures for Helmholtz resonance events are small relative to those for bubble oscillation events (Fig. 9f). Helmholtz resonance can also occur within an air cavity above the magma (e.g. Fee et al, 2010b; Goto and Johnson, 2011). We suggest the relatively large estimated bubble lengths (Fig. 9d) indicate an unusually deep magma level in the upper conduit and resonance occurred in an air cavity above the Strombolian explosions.

Laboratory experiments have shown that gas slugs occupy a large portion of the upper conduit with a thin magma film between the slug and conduit walls (e.g. James et al, 2006; Del Bello et al, 2012), therefore the maximum estimated bubble radii should be only slightly less than the conduit radius at the burst point (i.e. magma surface). Images of the vent captured by drone on the morning of 5 May suggested an upper conduit radius of approximately 3.5 m (Joël Ruch, pers. communication). Estimated bubble radii for both bubble oscillation and Helmholtz resonance models on 5 May fall beneath or close to this value (Fig. 8a, 9c). We also found larger maximum bubble radii on 18 May, suggesting an increase in conduit radius during the lava fountaining. This is supported by a steady increase in seismic tremor amplitudes during May 2021 (Fig. 4c, g; Eibl et al, 2022). Mechanical erosion of upper conduit and vents have been observed to affect acoustic frequencies during eruptions (e.g. Fee et al, 2017; Watson et al, 2020), therefore we surmise the same process occurred at Fagradalsfjall. We also suggest that a wider conduit radius in late May (Fig. 8a, e) could be a factor in explaining the shorter lava fountaining durations (Fig. 2c). Linear acoustic theory suggests a linear relationship between acoustic amplitudes and mass eruption rates (Woulff and McGetchin, 1976). Higher acoustic amplitudes recorded in late May relative to early May (Figs. 2, 4) therefore suggest higher fluxes of gas during each lava fountain event in the later period. Thus, a wider conduit allows similar or larger quantities of gas to migrate en masse to the surface in a shorter amount of time.

Constraints on the upper conduit dimensions from Strombolian explosion modelling can, in turn, be used to help define the Strouhal number St which connects

the peak frequency F_p, jet diameter D_j and jet velocity U_j via $St = f_p D_j / U_j$. Frequencies during peak lava fountaining ranged from 0.5 to 2 Hz, peaking at 1–2 Hz (Figs. 6b, 7b). Lava fountain heights H can be related to gas velocity v at the vent by $v = \sqrt{2gH}$ (Wilson, 1980). Peak lava fountain heights during early and late May ranged from 110 to 145 m (Fig. 5), giving peak gas velocities (i.e. jet velocities) of 46.4 to 53.3 $m \cdot s^{-1}$. Together with the maximum bubble radii found in early and late May (Fig. 8), we estimate St of 0.26–0.43 for the lava fountain sequence at Fagradalsfjall. These represent maximum values as we likely underestimate lava fountain heights since the camera image angle could not see the vent base (Fig. 1b). Nevertheless, these estimations fall within the range of St values previously estimated from volcanic jetting (Matoza et al, 2009; McKee et al, 2017), but lower than estimated for Stromboli volcano (1.2–1.8; Taddeucci et al, 2014). However, we note that peak acoustic frequencies at Stromboli were measured up to 305 Hz, hence the high St values. Finally, we note that peak acoustic frequencies during each event (red dots in Figs. 6b, 7b) weakly correlate with lava fountain heights, suggesting a relatively constant St value on short-term intervals.

6 Conclusions

Acoustic recordings can provide important constraints on the eruptive dynamics and source parameters of volcanic eruptions, but data from basaltic fissure eruptions with Hawaiian-style lava fountains are relatively rare. Here we present an account of acoustic data recorded by a sensor array during the lava fountain sequence of the 2021 Fagradalsfjall eruption in Iceland with analysis focused on activity in early and late May. We find that the array successfully tracked variations in event durations and repose intervals over time but was affected by wind noise. Relative acoustic energies of coherent acoustic detections in early May showed an upward trend in values which may be linked to increasing effusion rates. Detailed inspection of acoustics, and comparisons with seismic data and lava fountain height measurements, revealed a dynamic eruptive sequence during each event: acoustic tremor during peak lava fountaining was followed by a transition to Strombolian activity with distinct high-amplitude impulsive waveforms. We observe a divergence between acoustic and seismic amplitudes during each event, with the latter appearing to overestimate lava fountain durations. Jet noise similarity spectra fitting finds complex distributions of turbulent acoustics during each event, with changes of spectral shape and

frequency correlated with fountain height. Strombolian explosions are mostly composed of events that can be modelled by oscillations of bursting gas slugs at the top the magma column, with a minor number of events exhibiting Helmholtz resonance behaviour instead. Modelling of each source type finds maximum bubble radii of <3.5 m in early May and <4.5 m in late May, suggesting a widening of the upper conduit during the lava fountain activity. Finally, we propose that a wider conduit in late May, together with higher acoustic amplitudes, indicates higher gas fluxes through the conduit which resulted in briefer lava fountain events. Overall, this study demonstrates the value in incorporating acoustic microphones into future sensor deployments at basaltic fissure eruptions in Iceland and elsewhere through providing important constraints on eruption dynamics and upper conduit dimensions that may not be feasible otherwise.

Supplementary information. Supplementary materials include Figures S1–S9, a detailed description of lava fountain height estimation methodology, and a video of a lava fountain event on 11 May.

Authors' contributions. Oliver Lamb, Jonathan Lees, Michael Shore, and Stephen Lee initiated the study conception and design. Data collection was performed and supported by Oliver Lamb, Cécile Ducrocq and Kristín Jónsdóttir. Data analysis was performed by Oliver Lamb, Talfan Barnie and Julia Gestrich. The first draft of the manuscript was written by Oliver Lamb which all authors commented on. All authors read and approved the final manuscript.

Data availability. Acoustic data are available via the Incorporated Research Institutions for Seismology Data Management Center (https://ds.iris.edu/ds/nodes/dmc/) under the temporary network code XH. Station MER was part of the Icelandic Met Office seismic network and data is available upon request.

Acknowledgments. This research was performed while O. Lamb held an NRC Research Associateship award with the U.S. Army Research Laboratory/Army Research Office while based at the University of North Carolina at Chapel Hill. K. Jónsdóttir was supported by the Icelandic Research Fund via the IS-TREMOR project (217738-051). C. Ducrocq was supported by the NordVulk fellowship programme (2020). John Lyons provided helpful advice on deploying acoustic sensors near a fissure eruption and on modelling bubble oscillations. This paper benefited from various Python packages such as ObsPy (Krischer et al, 2015), Matplotlib (Hunter, 2007), and PyGMT (Uieda et al, 2021).

Appendix A Bubble modelling

A.1 Bubble oscillation model

The general equation for an oscillating bubble relates the kinetic energy exchange between a thin bubble cap and potential energy of the gas (Vergniolle and Brandeis, 1996):

$$0 = \ddot{\varepsilon} + \left(\frac{12\mu_l}{\rho_l R_{eq}^2}\right)\dot{\varepsilon} + \frac{P_{atm}}{\rho_l R_{eq} h_{eq}}\left[1 - \left(\frac{V_{eq}}{V_g}\right)^{\gamma}\right](1+\varepsilon)^2 \tag{A1}$$

where R_{eq} and V_{eq} are the bubble equilibrium radius and volume, respectively, h_{eq} is the bubble membrane thickness at equilibrium (0.15 m), P_{atm} is atmospheric pressure (10^5 Pa), ρ_l is the liquid density (2700 kg.m^{-3}), μ_l is the liquid viscosity (100 Pa·s), and V_g is equal to:

$$V_g = \frac{2\pi R^3}{3} + \pi R_o^2 L \tag{A2}$$

where R_o is the initial radius of the bubble; V_g is a function of the dimensionless bubble radius ε. Heat transfer within large bubbles is adiabatic (Plesset and Prosperetti, 1977), therefore internal bubble pressure will follow variations in volume with a ratio of specific heat γ, equal to 1.1 for hot gases (Lighthill, 1978). Bubble radius R can be described by its variation from the equilibrium radius R_{eq} (Vergniolle and Brandeis, 1996):

$$R = R_{eq}(1+\varepsilon) \tag{A3}$$

where:

$$R_{eq} = \left(\frac{3}{2}\right)^{\frac{1}{3}}\left[\left(\frac{2R_o^3}{3} + R_o^2 L\right)\left(1 + \frac{\Delta P}{P_{atm}}\right)^{\frac{1}{\gamma}} - R_o^2 L\right]^{\frac{1}{3}} \tag{A4}$$

in which L is the length of the cylindrical bubble within the conduit, and ΔP is the source pressure, or amount the bubble initially at rest at the magma-air interface is suddenly overpressured.

The pressure recorded at the sensor $p_{ac} - p_{air}$ at time t is (Vergniolle and Brandeis, 1996):

$$p_{ac} - p_{air} = \left[2\dot{R}^2(t - r/v) + R(t - r/v)\ddot{R}(t - r/v)\right]\frac{\rho_{air} R(t - r/v)}{r} \tag{A5}$$

where r is the source-receiver distance (0.8 km), v is sound velocity in air (340 m·s^{-1}), R is the bubble radius, and ρ_{air} is the air density (1.1 kg.m^{-1}). Therefore, calculation of synthetic pressure waveforms primarily depends on only three variables: ΔP, R_o, and L. A full technical discussion of the model can be found in Vergniolle and Brandeis (1996).

A.2 Helmholtz resonance modelling

During Helmholtz resonance, sound is produced by the motion of gas rushing from a small tube into an infinite space, where the tube length is equal to the thickness of the liquid layer (i.e. a hole in the bubble membrane). Sound emission is approximated by that of a piston mounted on an infinite baffle, producing sound as a monopole source in the far field (Spiel, 1992). For a piston emitting sound in a half-space (Vergniolle and Caplan-Auerbach, 2004):

$$p_{ac} - p_{air} = \frac{\rho_{air}\ddot{\xi}\pi R_{hole}^2}{2\pi r} \tag{A6}$$

where ξ is the displacement of air. If the resonator dimensions are small compared to the acoustic wavelength, the behaviour of an undriven Helmholtz resonator is:

$$0 = m_{helm}\ddot{\xi} + \kappa_{helm}\dot{\xi} + s_{helm}\xi \tag{A7}$$

where m_{helm}, κ_{helm}, and s_{helm} are the mass, the resistance coefficient, and the stiffness coefficient of the oscillator, respectively. These are defined as:

$$m_{helm} = \rho_{air}\epsilon S_{hole} \tag{A8}$$

$$\kappa_{helm} = \frac{\rho_{air}\omega^2 S_{hole}^2}{2\pi v} \tag{A9}$$

$$s_{helm} = \frac{\rho_{air}v^2 S_{hole}^2}{V_{helm}} \tag{A10}$$

where S_{hole} is the hole area, V_{helm} is the volume of the resonator, and ϵ is the effective length of the orifice. The oscillator effective length is longer than the geometrical length (i.e. the bubble membrane thickness, h_{eq}) because some of the air beyond the hole also moves (Spiel, 1992). The effective length ϵ corresponds essentially to end corrections of a flanged piston which are difficult to estimate since the behaviour of a gas about the hole is nonlinear (Vergniolle and Caplan-Auerbach, 2004). Spiel (1992) suggests a value of $8R_{hole}/3\pi \leq \epsilon \leq 16R_{hole}/3\pi$, therefore we use $\epsilon = 4R_{hole}/\pi$ as a representative value.

A damped harmonic solution can be defined as:

$$\xi = Ae^{-t/\tau}\cos(\omega t + \phi) \tag{A11}$$

$$\dot{\xi} = -Ae^{-t/\tau}[\omega\sin(\omega t + \phi) + \cos(\omega t + \phi)/\tau] \tag{A12}$$

$$\ddot{\xi} = -\omega^2 Ae^{-t/\tau}\cos(\omega t + \phi) \tag{A13}$$

where A and ϕ are arbitrary constants to be determined by initial conditions. The relaxation time τ and the radian frequency ω are:

$$\tau = \frac{2m_{helm}}{\kappa_{helm}} \tag{A14}$$

$$\omega = \sqrt{\omega_0^2 - \frac{1}{\tau^2}} \tag{A15}$$

where ω_0 is the radian frequency without damping, defined as (Vergniolle and Caplan-Auerbach, 2004):

$$\omega_0 = v\sqrt{\frac{S_{hole}}{\epsilon V_{helm}}} \tag{A16}$$

The initial force on the mass of resonating air will be $\Delta P S_{hole}$, the initial speed of the mass will be zero, and the mass of the rupturing bubble membrane will be ignored. These conditions lead to:

$$\phi = \arctan\left[\frac{-1}{\omega\tau}\right] \tag{A17}$$

$$A = -\frac{\Delta P}{\rho_{air}\epsilon\omega^2\cos\phi} \tag{A18}$$

Finally, the following equations given by Temkin (1981) and Spiel (1992) are adapted for a cylindrical bubble of length L with a volume V_{helm}:

$$V_{helm} = \frac{2\pi R^3}{3} + \pi R^2 L \tag{A19}$$

$$S_{hole} = \pi R_{hole}^2 \tag{A20}$$

where R_{hole} is the radius of the hole, which is assumed to be set at its value instantaneously and remains constant over time. Ultimately, calculation of synthetic pressure waveforms from Helmholtz resonance primarily depends on only three variables: ΔP, R_{hole}, and L.

References

Barsotti S, Parks MM, Pfeffer MA, et al (2022) The Eruption in Fagradalsfjall (2021, Iceland): How The Operational Monitoring and The Volcanic Hazard Assessment Contributed to Its Safe Access. https://doi.org/10.21203/rs.3.rs-1453832/v1

Cannata A, Montalto P, Privitera E, et al (2009) Tracking eruptive phenomena by infrasound: May 13, 2008 eruption at Mt. Etna. Geophysical Research Letters 36(5). https://doi.org/10.1029/2008GL036738

Cannata A, Sciotto M, Spampinato L, et al (2011) Insights into explosive activity at closely-spaced eruptive vents using infrasound signals: Example of Mt. Etna 2008 eruption. Journal of Volcanology and Geothermal Research 208(1–2):1–11. https://doi.org/10.1016/j.jvolgeores.2011.09.003

Del Bello E, Llewellin EW, Taddeucci J, et al (2012) An analytical model for gas overpressure in slug-driven explosions: Insights into Strombolian volcanic eruptions. Journal of Geophysical Research: Solid Earth 117(B2). https://doi.org/10.1029/2011JB008747

Eibl EPS, Thordarson T, Höskuldsson Á, et al (2022) Evolving Shallow-conduit Container Affects the Lava Fountaining during the 2021 Fagradalsfjall Eruption, Iceland. https://doi.org/10.21203/rs.3.rs-1453738/v1

Fee D, Matoza RS (2013) An overview of volcano infrasound: From hawaiian to plinian, local to global. Journal of Volcanology and Geothermal Research 249:123–139. https://doi.org/10.1016/j.jvolgeores.2012.09.002

Fee D, Garces M, Steffke A (2010a) Infrasound from Tungurahua Volcano 2006–2008: Strombolian to Plinian eruptive activity. Journal of Volcanology and Geothermal Research 193(1–2):67–81. https://doi.org/10.1016/j.jvolgeores.2010.03.006

Fee D, Garcés M, Patrick M, et al (2010b) Infrasonic harmonic tremor and degassing bursts from Halema'uma'u Crater, Kilauea Volcano, Hawaii. Journal of Geophysical Research 115(B11):B11,316. https://doi.org/10.1029/2010JB007642

Fee D, Garces M, Orr T, et al (2011) Infrasound from the 2007 fissure eruptions of Kīlauea Volcano, Hawai'i. Geophysical Research Letters 38(6). https://doi.org/10.1029/2010GL046422

Fee D, McNutt SR, Lopez TM, et al (2013) Combining local and remote infrasound recordings from the 2009 Redoubt Volcano eruption. Journal of Volcanology and Geothermal Research 259:100–114. https://doi.org/10.1016/j.jvolgeores.2011.09.012

Fee D, Haney MM, Matoza RS, et al (2017) Volcanic tremor and plume height hysteresis from Pavlof Volcano, Alaska. Science 355(6320):1–5. https://doi.org/10.1126/science.aah6108

Gestrich JE, Fee D, Matoza RS, et al (2021) Fitting Jet Noise Similarity Spectra to Volcano Infrasound Data. Earth and Space Science https://doi.org/10.1029/2021EA001894

Goto A, Johnson JB (2011) Monotonic infrasound and Helmholtz resonance at Volcan Villarrica (Chile). Geophysical Research Letters 38(6):1–5. https://doi.org/10.1029/2011GL046858

Hunter JD (2007) Matplotlib: A 2D Graphics Environment. Computing in Science & Engineering 9(3):90–95. https://doi.org/10.1109/MCSE.2007.55

James MR, Lane SJ, Chouet BA (2006) Gas slug ascent through changes in conduit diameter: Laboratory insights into a volcano-seismic source process in low-viscosity magmas. Journal of Geophysical Research: Solid Earth 111(5):1–25. https://doi.org/10.1029/2005JB003718

Johnson JB, Ripepe M (2011) Volcano infrasound: A review. Journal of Volcanology and Geothermal Research 206(3–4):61–69. https://doi.org/10.1016/j.jvolgeores.2011.06.006

Krischer L, Megies T, Barsch R, et al (2015) ObsPy: a bridge for seismology into the scientific Python ecosystem. Computational Science & Discovery 8(1):1–17. https://doi.org/10.1088/1749-4699/8/1/014003

Lighthill M (1978) Waves in Fluids. Cambridge University Press

Lyons JJ, Haney MM, Fee D, et al (2019) Infrasound from giant bubbles during explosive submarine eruptions. Nature Geoscience 12(11):952–958. https://doi.org/10.1038/s41561-019-0461-0

Lyons JJ, Dietterich HR, Patrick MP, et al (2021) High-speed lava flow infrasound from Kīlauea's fissure 8 and its utility in monitoring effusion rate. Bulletin of Volcanology 83(11):66. https://doi.org/10.1007/s00445-021-01488-7

Marcillo O, Johnson JB, Hart D (2012) Implementation, characterization, and evaluation of an inexpensive low-power low-noise infrasound sensor based on a micromachined differential pressure transducer and a mechanical filter. Journal of Atmospheric and Oceanic Technology 29(9):1275–1284. https://doi.org/10.1175/JTECH-D-11-00101.1

Matoza RS, Fee D, Garcés MA, et al (2009) Infrasonic jet noise from volcanic eruptions. Geophysical Research Letters 36(L08303). https://doi.org/10.1029/2008GL036486

Matoza RS, Fee D, Neilsen TB, et al (2013) Aeroacoustics of volcanic jets: Acoustic power estimation and jet velocity dependence. Journal of Geophysical Research: Solid Earth 118(12):6269–6284. https://doi.org/10.1002/2013JB010303

McKee K, Fee D, Yokoo A, et al (2017) Analysis of gas jetting and fumarole acoustics at Aso Volcano, Japan. Journal of Volcanology and Geothermal Research 340:16–29. https://doi.org/10.1016/j.jvolgeores.2017.03.029

Parfitt EA (2004) A discussion of the mechanisms of explosive basaltic eruptions. Journal of Volcanology and Geothermal Research 134(1–2):77–107. https://doi.org/10.1016/j.jvolgeores.2004.01.002

Patrick MR, Dietterich HR, Lyons JJ, et al (2019) Cyclic lava effusion during the 2018 eruption of Kīlauea Volcano. Science 366(6470). https://doi.org/10.1126/science.aay9070

Pedersen GBM, Belart JMC, Óskarsson BV, et al (2021) Volume, effusion rate, and lava transport during the 2021 Fagradalsfjall eruption: Results from near real-time photogrammetric monitoring. https://doi.org/10.1002/essoar.10509177.1

Plesset MS, Prosperetti A (1977) Bubble Dynamics and Cavitation. Annual Review of Fluid Mechanics 9(1):145–185. https://doi.org/10.1146/annurev.fl.09.010177.001045

Porter C, Morin P, Howat I, et al (2018) ArcticDEM. https://doi.org/10.7910/DVN/OHHUKH

Raspet R, Webster J (2015) Wind noise under a pine tree canopy. The Journal of the Acoustical Society of America 137(2):651–659. https://doi.org/10.1121/1.4906587

Seiner J (1984) Advances in high speed jet aeroacoustics. In: 9th Aeroacoustics Conference. American Institute of Aeronautics and Astronautics, https://doi.org/10.2514/6.1984-2275

Spiel DE (1992) Acoustical Measurements of Air Bubbles Bursting at a Water Surface: Bursting Bubbles as Helmholtz Resonators. Journal of Geophysical Research

97(C7):11,443–11,452. https://doi.org/10.1029/92JC00982

Szuberla CAL, Olson JV (2004) Uncertainties associated with parameter estimation in atmospheric infrasound arrays. The Journal of the Acoustical Society of America 115(1):253–258. https://doi.org/10.1121/1.1635407

Sæmundsson K, Sigurgeirsson MA, Friðleifsson GO (2020) Geology and structure of the Reykjanes volcanic system, Iceland. Journal of Volcanology and Geothermal Research 391:106,501. https://doi.org/10.1016/j.jvolgeores.2018.11.022

Taddeucci J, Sesterhenn J, Scarlato P, et al (2014) High-speed imaging, acoustic features, and aeroacoustic computations of jet noise from Strombolian (and Vulcanian) explosions. Geophysical Research Letters 41(9):3096–3102. https://doi.org/10.1002/2014GL059925

Tam C, Golebiowski M, Seiner J (1996) On the two components of turbulent mixing noise from supersonic jets. In: Aeroacoustics Conference. American Institute of Aeronautics and Astronautics, https://doi.org/10.2514/6.1996-1716

Tam CK (1998) Jet Noise: Since 1952. Theoretical and Computational Fluid Dynamics 10(1–4):393–405. https://doi.org/10.1007/s001620050072

Tam CKW (2019) A phenomenological approach to jet noise: the two-source model. Philosophical Transactions of the Royal Society A: Mathematical, Physical and Engineering Sciences 377(2159):20190,078. https://doi.org/10.1098/rsta.2019.0078

Temkin S (1981) Elements of acoustics. Wiley New York

Uieda L, Tian D, Leong WJ, et al (2021) PyGMT: A Python interface for the Generic Mapping Tools. https://doi.org/10.5281/zenodo.5607255

Vergniolle S, Brandeis G (1996) Strombolian explosions: 1. A large bubble breaking at the surface of a lava column as a source of sound. Journal of Geophysical Research: Solid Earth 101(B9):20,433–20,447. https://doi.org/10.1029/96JB01178

Vergniolle S, Caplan-Auerbach J (2004) Acoustic measurements of the 1999 basaltic eruption of Shishaldin volcano, Alaska 2. Precursor to the Subplinian phase. Journal of Volcanology and Geothermal Research 137(1–3):135–151. https://doi.org/10.1016/j.jvolgeores.2004.05.004

Vergniolle S, Ripepe M (2008) From Strombolian explosions to fire fountains at Etna Volcano (Italy): what do we learn from acoustic measurements? Geological Society, London, Special Publications 307(1):103–124. https://doi.org/10.1144/SP307.7

Vergniolle S, Brandeis G, Mareschal JC (1996) Strombolian explosions. 2. Eruption dynamics determined from acoustic measurements. Journal of Geophysical Research 101(B9):20,449–20,446

Vergniolle S, Boichu M, Caplan-Auerbach J (2004) Acoustic measurements of the 1999 basaltic eruption of Shishaldin volcano, Alaska 1. Origin of Strombolian activity. Journal of Volcanology and Geothermal Research 137(1–3):109–134. https://doi.org/10.1016/j.jvolgeores.2004.05.003

Viswanathan K (2009) Mechanisms of Jet Noise Generation: Classical Theories and Recent Developments. International Journal of Aeroacoustics 8(4):355–407. https://doi.org/10.1260/147547209787548949

Watson LM, Johnson JB, Sciotto M, et al (2020) Changes in Crater Geometry Revealed by Inversion of Harmonic Infrasound Observations: 24 December 2018 Eruption of Mount Etna, Italy. Geophysical Research Letters 47(19). https://doi.org/10.1029/2020GL088077

Wilson L (1980) Relationships between pressure, volatile content and ejecta velocity in three types of volcanic explosion. Journal of Volcanology and Geothermal Research 8(2–4):297–313. https://doi.org/10.1016/0377-0273(80)90110-9

Witt T, Walter TR (2017) Video monitoring reveals pulsating vents and propagation path of fissure eruption during the March 2011 Pu'u 'Ō'ō eruption, Kilauea volcano. Journal of Volcanology and Geothermal Research 330:43–55. https://doi.org/10.1016/j.jvolgeores.2016.11.012

Woulff G, McGetchin TR (1976) Acoustic noise from volcanoes: Theory and experiment. Geophysical Journal International 45(3):601–616. https://doi.org/10.1111/j.1365-246X.1976.tb06913.x